



## Full paper

# Ultrafine, high-loading and oxygen-deficient cerium oxide embedded on mesoporous carbon nanosheets for superior lithium–oxygen batteries

Lianbang Wang<sup>a,1</sup>, Siyuan Chen<sup>a,1</sup>, Jinpei Hei<sup>a</sup>, Rui Gao<sup>b</sup>, Liu Liu<sup>a</sup>, Liwei Su<sup>a,\*\*</sup>, Gaoran Li<sup>b,\*\*\*</sup>, Zhongwei Chen<sup>b,\*</sup>

<sup>a</sup> State Key Laboratory Breeding Base of Green Chemistry-Synthesis Technology, College of Chemical Engineering, Zhejiang University of Technology, Hangzhou, 310014, China

<sup>b</sup> Department of Chemical Engineering, University of Waterloo, Waterloo, ON, N2L 3G1, Canada



## ARTICLE INFO

## Keywords:

Lithium-oxygen battery  
Cerium oxide  
Mesoporous carbon  
Oxygen deficiency  
Crystal size  
High loading

## ABSTRACT

The exploitation of advanced cathode materials for rechargeable lithium-oxygen batteries (LOBs) are receiving tremendous attentions worldwide. However, the rational design and regulation on their chemical component and architecture, particularly with regard to the tradeoff between catalyst size and mass loading, toward efficient oxygen catalysis and superior LOB performance are still critical and challenging. Herein, we developed a unique composite of oxygen-deficient cerium oxide (CeO<sub>x</sub>) embedded on mesoporous carbon (MC) with a concurrent fulfillment of ultrafine crystal (1.98 nm in average) and high mass loading (up to 43.8 wt%), as cathode catalyst for superior LOBs. The ultrafine CeO<sub>x</sub> distribution sufficiently exposes the catalytic sites, while the highly porous architecture ensures facile electron/mass transfer, thus synergistically contributing to a fast and efficient oxygen catalysis. As a result, the optimized CeO<sub>x</sub>/MC enables significantly reduced overpotentials for oxygen redox reactions, ultrahigh capacity of 12753 mAh g<sup>-1</sup> and Coulombic efficiency of 92.1% at ultimate-capacity charge-discharge, as well as decent cyclability over 55 cycles at limited-capacity (1000 mAh g<sup>-1</sup>) cycling in LOBs. This work offers an insightful exploration on advanced catalyst materials with simultaneous ultras-small crystal size and high mass loading, holding a great potential for material engineering in LOBs and other related fields.

## 1. Introduction

Rechargeable lithium-oxygen batteries (LOBs), as an advanced energy storage technology, have been attracting tremendous research enthusiasm in both academic and industrial communities due to the intriguingly high energy densities up to 11.4 kWh kg<sup>-1</sup> and 6.1 kWh L<sup>-1</sup> [1–5]. Although great progress has been achieved over the past few decades, key challenges such as high overpotentials, low lifespan, poor round-trip efficiency and unsatisfactory rate capability are still haunting and calling for serious solutions [6,7]. According to the "two-phase reaction zone" theory, oxygen reduction reaction (ORR) and oxygen evolution reaction (OER) mainly occur at the interface between electrolyte and catalyst [8]. However, the multi-phase-involved and multi-electron-transfer processes of ORR/OER determine their intrinsically sluggish kinetics, while the low solubility of oxygen in electrolyte

seriously limits its contact with catalytic surface and further impedes the oxygen redox reactions. One conceivable solution lies in the enhancement of oxygen solubility by e.g., altering the electrolyte system, while the majority of the research efforts have been focused on the development of advanced materials with higher oxygen capturability and catalytic activity to overcome the intrinsic kinetic demerits [9,10]. Advanced catalyst materials that promote efficient and facile oxygen reactions are highly desired in Li–O<sub>2</sub> chemistry, which determines the battery lifespan and rate capability.

The past few decades have witnessed a flourishing development of multifarious catalyst materials for ORR and OER, including precious metals (Pt, Pd, Ru, etc.) [11–13], non-precious metals (Fe, Co, Ni, etc.) [14–16], metal compounds (RuO<sub>2</sub>, TiO<sub>2</sub>, Co<sub>3</sub>O<sub>4</sub>, etc.) [17–19], as well as carbon materials with various heteroatoms [20,21]. Among them, ceria (CeO<sub>2</sub>) has shown a particular promise as cathode catalyst in LOBs. CeO<sub>2</sub>

\* Corresponding author.

\*\* Corresponding author.

\*\*\* Corresponding author.

E-mail addresses: [suliwei@zjut.edu.cn](mailto:suliwei@zjut.edu.cn) (L. Su), [lgr19890725@gmail.com](mailto:lgr19890725@gmail.com) (G. Li), [zhwchen@uwaterloo.ca](mailto:zhwchen@uwaterloo.ca) (Z. Chen).

<sup>1</sup> These authors contributed equally to this work.

could serve as “oxygen buffer” to reversibly absorb and release  $O_2$  as expressed:  $CeO_2 \leftrightarrow CeO_x + (2-x)/2O_2$  ( $1.5 < x < 2$ ), contributing to an enhanced mobility of oxygen species and significant improvement in overall LOB performance [22]. The lattice oxygen in  $CeO_2$  is relatively active and highly mobile, which also facilitates the formation of oxygen vacancies [23]. Thus, oxygen-deficient cerium oxide ( $CeO_x$ ) is highly accessible with a favorable oxygen transfer capability. Though deviating from the stoichiometry, defective  $CeO_x$  could maintain ordered crystalline structure to a considerable extent, while more importantly, oxygen vacancies are anticipated to provide extra active sites for oxygen catalysis [24–26].

Despite the convincing advantages, the poor conductivity of  $CeO_x$  is restricting its applications, which calls for the implementation of conductive substrate. In this regard, porous carbons deliver high specific area and good conductivity, serving as promising substrates to support the electron/mass transfer as well as the catalytic process on  $CeO_x$  [27–29]. In this consideration, the combination of  $CeO_x$  and mesoporous carbon (MC) could be a feasible solution to efficient cathode catalyst for LOBs. It should be noted that the crystal size and mass loading of  $CeO_x$  on carbon substrates seriously affect its catalytic ability [30,31]. Smaller size is beneficial for sufficient exposure of active surface, while the higher catalyst loading contributes to higher mass activity. However, the combination of them are generally hard to achieve due to the easy agglomeration of high-content  $CeO_x$  upon the synthesis. Therefore, rational material design and regulation that concurrently realize the ultrafine crystal size (particularly  $< 3$  nm) and high mass loading are highly favorable for boosting LOB performance yet still challenging to implement.

In this contribution, we developed a unique composite catalyst with ultrafine  $CeO_x$  nanoparticles embedded on MC nanosheets (denoted as  $CeO_x/MC$ ) with an unprecedentedly high mass loading up to 43.8 wt%. The  $CeO_x/MC$  was prepared through a facile impregnation and carbonization process, where corn stalks serve as not only the carbon source but also the robust confining framework to prevent the agglomeration of  $CeO_x$ . The evolution of  $x$  value (1.813–1.788) in  $CeO_x$  and the according crystal size (1.98–9.62 nm) were comprehensively studied along with the variation of calcination temperature. As the optimized sample,  $CeO_x/MC-600$  combines the ultrafine  $CeO_x$  distribution and highly porous architecture, which facilitates sufficient exposure of catalytic sites, expedite electron/mass transfers and uniform phase nucleation, leading to the best LOB battery performance, i.e., the smallest ORR/OER overpotential, highest capacity and coulombic efficiency at ultimate-capacity test as well as the highest cyclability at limited-capacity cycling.

## 2. Experimental

### 2.1. Preparation of $CeO_x/MC$

For the preparation of  $CeO_x/MC$ , corn stalks were collected from farms and used as the carbon resource. The corn stalks were successively crushed into small particles, soaked in diluted  $H_2SO_4$  solution (1.5 wt%) at 95 °C for 1 h, washed with deionized water to neutrality and dried at 45 °C for 12 h before use. In typical synthesis, 20 mg pre-treated corn stalks were immersed in a 50 mM cerium acetate solution. 30 min sonication and 30 min vacuum treatment were alternated and repeated 2 times in order to remove the air inside the corn stalk and ensure the uniform impregnation. The as-prepared precursor was dried at 60 °C for 24 h before calcinating at high temperature (600, 700, 800 and 900 °C) for 4 h in Ar flow to yield the  $CeO_x/MC$  product. The obtained samples were denoted as  $CeO_x/MC-X$  ( $X = 600, 700, 800$  and  $900$ ) accordingly. For comparison, pure MC and low-loading sample (denoted as 1 mM  $CeO_x/MC-600$ ) were also prepared by using no cerium and diluted cerium acetate solution, respectively, under similar conditions (calcinating at 600 °C).

### 2.2. Material characterizations

Scanning electron microscopy (SEM, Hitachi S-4700 at 15 kV), transmission electron microscopy (TEM, Tecnai G2 F30 S-Twin), and high-resolution transmission electron microscopy (HRTEM) were used to investigate the structure and morphology of the prepared materials. The crystalline structures and surface chemistries of the samples were studied by X-ray diffraction (XRD, PANalytical X'Pert Pro X-ray with Cu K $\alpha$  radiation,  $\lambda = 1.5418$  Å, scanning rate: 2° min<sup>-1</sup>), energy-dispersive X-ray spectroscopy (EDX, Tecnai G2 F30 S-Twin), and X-ray photoelectron spectroscopy (XPS, Kratos Axis DLD spectrometer with monochromatic Al K $\alpha$  radiation,  $h\nu = 1486.6$  eV). Thermogravimetric analysis (TGA, PerkinElmer) was used to analyze the composition of the samples. Brunauer-Emmett-Teller (BET, Conta AUTOSORB IQ) method was used to investigate the porous structures.

### 2.3. Electrochemical measurements

The electrochemical performances of the as-prepared  $CeO_x/MC$  and pure MC were evaluated in two-electrode configuration. Carbon paper (0.1 mm thick, HCP010 N, Shanghai Hesen Electric Co., Ltd., China) was used as the current collector and gas diffusion layer of cathode catalysts. For the fabrication of oxygen electrodes,  $CeO_x/MC-X$  ( $X = 600, 700, 800$  and  $900$ ) and polyvinylidene fluoride (PVDF) (9:1 w/w) were uniformly dispersed in N-methyl-2-pyrrolidinone (NMP) to obtain a uniform slurry, which was then pasted onto the surface of carbon paper and dried at 120 °C in vacuum. The mass loading of active material is approximately 0.5 mg per tablet. The CR2032 coin cells were assembled in glove box filled with high-purity Ar ( $H_2O$  and  $O_2 < 1$  ppm) by using the as-prepared oxygen electrode as cathode, lithium foil (China Energy Lithium Co., LTD) as counter and reference electrode, and glass fiber (Whatman GF/D) as the separator. The electrolyte contains 1 M lithium trifluoromethanesulfonate (LiTFSI) in dimethylsulfoxide (DMSO). Galvanostatic charge/discharge test was performed by a LAND test system (CT2001A) in a self-designed oxygen-filled glass bottle. Electrochemical impedance spectroscopy (EIS) analysis was carried out by using a CHI660B electrochemical workstation in the frequency range of 0.01 Hz–100 kHz with an amplitude of 5 mV. Cyclic voltammetry (CV) measurement was also performed by CHI660B workstation at a scanning rate of 0.1 mV s<sup>-1</sup>.

## 3. Results and discussion

Fig. 1 schematically illustrates the preparation of  $CeO_x/MC$  composites for LOBs. Corn stalks were collected and pretreated, serving as the carbon source as well as the hosting matrix for Ce impregnation (see details in Experimental). The obtained precursors were directly subject to calcination under varied temperatures to yield the product  $CeO_x/MC$  with different microstructures. This method presents a facile and cost-effective pathway toward  $CeO_x/MC$  composite with tunable physicochemical properties, holding a good potential for scale-up production and wide applications.

To determine the chemical components of the  $CeO_x/MC$  samples, XRD, TGA, and XPS characterizations were conducted as shown in Fig. 2. In the XRD patterns (Fig. 2A), all the diffraction peaks of  $CeO_x/MC-X$  ( $X = 600, 700$  and  $800$ ) can be well indexed to the standard face centered cubic (FCC)  $CeO_2$  (JCPDS No. 34-0394, space group: Fm-3m). The main peaks at 28.6°, 33.1°, 47.5° and 56.3° correspond to the (111), (200), (220) and (311) lattice planes, respectively [32]. However,  $CeO_x/MC-900$  presents three extra peaks at 26.3°, 43.9° and 55.7°, which can be assigned to the (222), (044) and (543) planes respectively of the body centered cubic (BCC)  $CeO_{2-x}$  (JCPDS No. 49-1415, space group: Ia3,  $x \geq 0.5$ ) [33]. Moreover, a small peak can be also observed emerging at 30.4°, referring to the (011) plane of hexagonal  $Ce_2O_3$  (JCPDS No. 44-1086, space group: P321). The emergence of crystalline impurities could be ascribed to the excessive reduction of  $CeO_x$  under

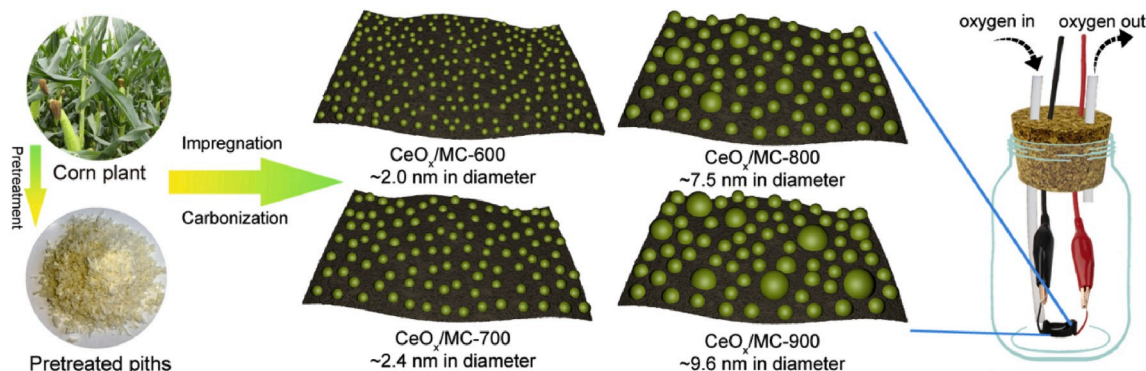


Fig. 1. Schematic diagram of the preparation of  $\text{CeO}_x/\text{MC-X}$  samples.

900 °C. In addition, a continuous decrease in half-peak width of the XRD peaks can be noticed for the obtained  $\text{CeO}_x/\text{MCs}$  along with the increase of calcination temperature, implying the continuous growth of  $\text{CeO}_x$  particles in the products [34].

TGA was performed to estimate the composition of  $\text{CeO}_x/\text{MC-600}$  as shown in Fig. 2B. The mass loss of 4.4% before 200 °C is attributed to the evaporation of absorbed moisture, while the 53.7% weight loss at 200–355 °C is due to the combustion of MC. On this basis, the content of  $\text{CeO}_x$  in  $\text{CeO}_x/\text{MC-600}$  is determined ca. 43.8 wt%, which to the best of our knowledge, is the highest mass loading ever reported for sub-3 nm  $\text{CeO}_x$  on carbon substrates [35–39]. Similarly, TGA was also performed for  $\text{CeO}_x/\text{MC}$  under different calcination temperatures as shown in Fig. S1. Similar profiles with close residual mass can be observed for these samples, revealing their similar  $\text{CeO}_x$  contents (42.83, 41.85 and 42.31 wt % for  $\text{CeO}_x/\text{MC-700}$ , 800 and 900, respectively). This result indicates that the calcination temperature imposes limited influence on  $\text{CeO}_x$  content in the product. By contrast, the cerium concentration in the impregnation solution affects more significantly, e.g., that 1 mM  $\text{CeO}_x/\text{MC-600}$  obtained from diluted Ce precursor solution (1 mM) exhibits a lower  $\text{CeO}_x$  content of ~10 wt % (Fig. S1). Although higher loading is generally desired for enhanced mass activity, the increase of concentration will decrease the utilization of precursor, thus raising the cost and damaging the synthesis efficiency as demonstrated in Fig. S2. Meanwhile, the excessively high concentration will also induce the  $\text{CeO}_x$  agglomeration in the product with a resultant recession in specific activity (Fig. S3). Based on these considerations, the cerium acetate concentration of 50 mM was employed as the appropriate value for  $\text{CeO}_x/\text{MC}$  fabrication.

The surface chemistry of the obtained  $\text{CeO}_x/\text{MC}$  was analyzed by XPS as shown in Fig. 2 and Fig. S4. The survey spectrum confirms the existence of Ce, O and C in the composite (Fig. 2C). The C 1s core level spectrum of  $\text{CeO}_x/\text{MC-600}$  shows three deconvoluted peaks, corresponding to C–C (284.8 eV), C–O (286.01 eV) and O=C=O (288.75 eV) structures, respectively (Fig. 2D) [40,41]. Fig. 2E reveals the different O states in  $\text{CeO}_x/\text{MC-600}$ , where the O1 (530 eV), O2 (531.4 eV), O3 (533.0 eV) and O4 (534.1 eV) refer to the lattice oxygen, oxygen vacancy, hydroxyl groups and oxygen-containing functional groups on MC, respectively, suggesting the oxygen-deficient nature of  $\text{CeO}_x$  [42, 43]. The Ce 3d spectrum further confirms the non-stoichiometry in the obtained composite by showing various Ce states in Fig. 2F. The v and u peaks signify the 3d<sub>5/2</sub> and 3d<sub>3/2</sub> levels, respectively. The v<sub>0</sub>, v<sub>1</sub>, u<sub>0</sub> and u<sub>1</sub> peaks are ascribed to the primary photoemission of  $\text{Ce}^{3+}$ , while the rest v and u peaks are assigned to  $\text{Ce}^{4+}$  [44,45]. By calculating the peak area of  $\text{Ce}^{3+}$  and  $\text{Ce}^{4+}$ , the x value in  $\text{CeO}_x/\text{MC-600}$  can be estimated ca. 1.813, validating the oxygen deficiency in the product. Similarly, x values in  $\text{CeO}_x/\text{MC-700}$ , 800 and 900 are ca. 1.806, 1.798 and 1.788, respectively, deduced from the according XPS spectra as shown in Fig. S4, which suggest the continuous reduction of Ce as well as the slight increase of oxygen vacancies along with the increase of

calcination temperature. Additionally, the commercial cerium oxide as a control sample shows significantly weakened v<sub>1</sub> and u<sub>1</sub> peaks, demonstrating its less oxygen vacancies with a x value ca. 1.882 compared with the as-prepared samples (Fig. S4A). The XPS fitting parameters are listed in Tables S1 and S2.

Despite the impact on oxygen deficiency, it is notable that the temperature variation imposes great influence on the crystal size of  $\text{CeO}_x$ . The crystal size generally depends on the diffusivity of metal atoms in the carbon medium upon the calcination process, i.e., higher diffusivity leads to bigger particles [46]. Given this, the size of  $\text{CeO}_x$  nanocrystal can be delicately regulated by simply adjusting the calcination temperature in our case. Fig. 3 shows the typical TEM images and crystal size distributions of  $\text{CeO}_x/\text{MC-X}$  (X = 600, 700, 800 and 900). Apparently, the  $\text{CeO}_x$  nanocrystals become increasingly observable with a largening size along with the increase of calcination temperature from 600 to 900 °C. The particle size of  $\text{CeO}_x$ -600 is concentrated in 1.6–2.4 nm with an average size of 1.98 nm, while 97% of  $\text{CeO}_x$  is smaller than 3 nm (Fig. 3A and B). By comparison,  $\text{CeO}_x$ -700 undergoes a slightly increase in particle size with a concentration range of 1.7–2.8 nm and an average diameter of 2.43 nm. Meanwhile, a relatively decreased percentage (82%) of crystals are smaller than 3 nm (Fig. 3C and D). As temperature further increases to 800 and 900 °C, serious agglomeration can be observed in  $\text{CeO}_x/\text{MC-800}$  and 900, leading to significantly larger particles in average diameter of 7.47 and 9.62 nm, respectively (Fig. 3E–H). Upon the calcination, the corn stalks and the as-derived carbon matrix establish a robust framework that confines the impregnated Ce-species, which subsequently regulates the diffusion behavior of  $\text{CeO}_x$  and mitigates their agglomeration. Higher temperature motivates the diffusivity of  $\text{CeO}_x$  and contributes to the growth of crystal size, whereas excessively high temperatures such as 800 and 900 °C fail the meticulous size regulation and lead to the considerable crystal agglomeration with broadened size distribution. As a result, the  $\text{CeO}_x/\text{MC-600}$  delivers the smallest crystal size and the most uniform distribution, which is expected with the best oxygen catalysis performance.

To further study the morphological and microstructural features of  $\text{CeO}_x/\text{MC-600}$ , SEM, HRTEM and EDX mapping were carried out as shown in Fig. 4, Figs. S5 and S6. The SEM images demonstrate that  $\text{CeO}_x/\text{MC-600}$  is composed of large-area nanosheets (10–100 μm in width) with relatively smooth surface (Fig. 4A–C). Accordingly,  $\text{CeO}_x$  particles can be hardly seen in relatively low-magnification TEM image in Fig. 4D. Whereas at higher magnifications (Fig. 4E and F),  $\text{CeO}_x$  nanocrystals can be clearly observed in forms of black dots in uniform sub-3 nm size and massive distribution. The crystallinity of  $\text{CeO}_x$  is confirmed by the lattice fringe with interplanar space of 0.31 nm, which corresponds to the (111) plane of FCC cerium oxide. Moreover, the HRTEM observation also demonstrates the typically microcrystal and polycrystal structures in  $\text{CeO}_x/\text{MC-600}$ , where considerable point defects and grain boundaries can be perceived, further confirming the

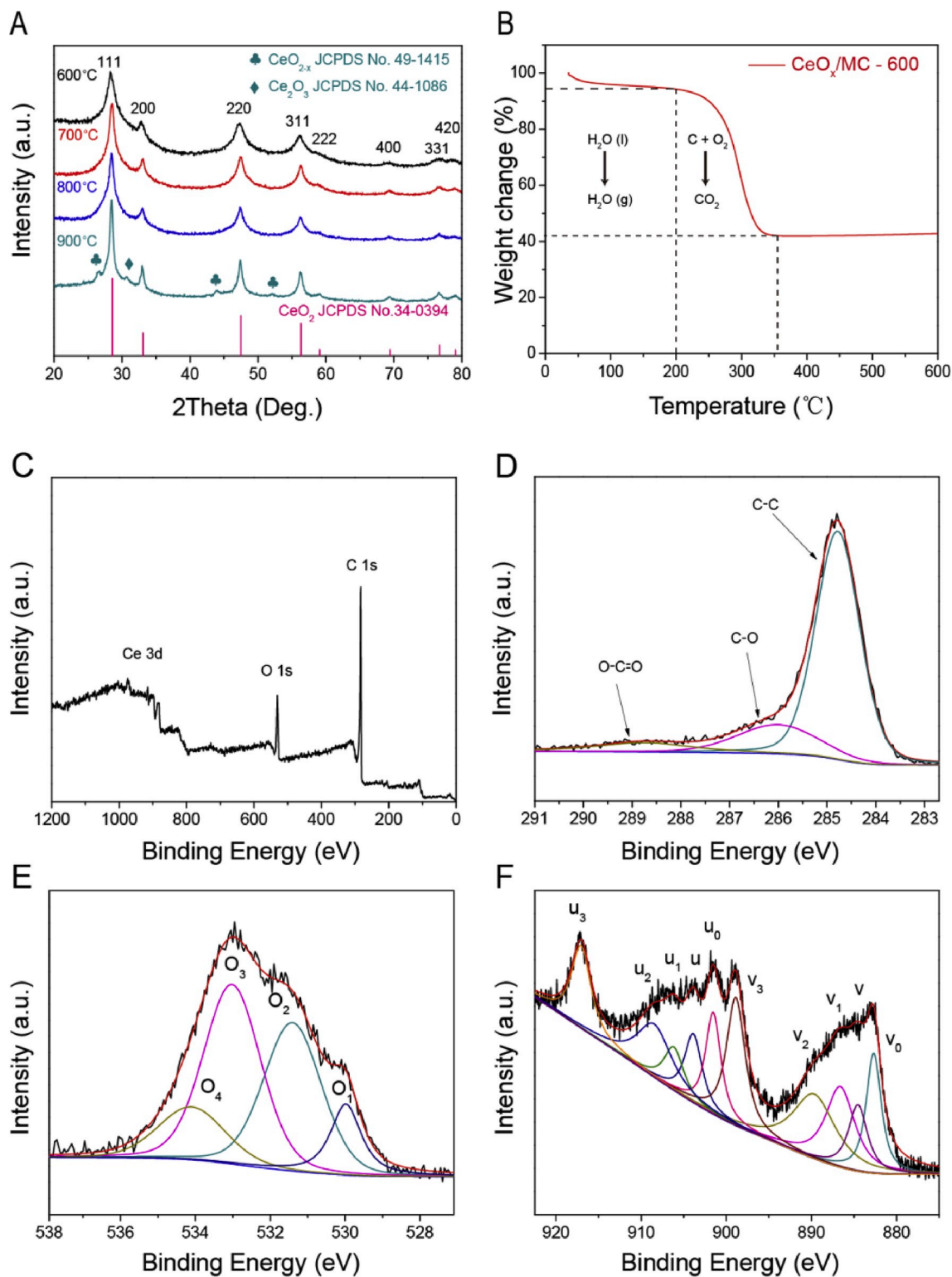


Fig. 2. (A) XRD patterns of  $\text{CeO}_x/\text{MC-X}$  ( $X = 600, 700, 800$  and  $900$ ); (B) TGA curve of  $\text{CeO}_x/\text{MC-600}$  in air; XPS (C) survey, (D) C 1s, (E) O 1s and (F) Ce 3d spectra of  $\text{CeO}_x/\text{MC-600}$ .

defective nature of the product (Fig. S5). The HADDF-STEM and EDX mapping were also collected as shown in Fig. S6, which reveals the uniform distribution of  $\text{CeO}_x$  within the MC matrix. The ultrasmall size and uniform distribution of the  $\text{CeO}_x$  nanocrystals are mainly attributed to the spatial confinement effect by the corn stalk substrate, which strongly adsorbs and immobilizes Ce species against agglomeration.

Apart from that, the porosity characters of samples were investigated

by  $\text{N}_2$  adsorption-desorption measurement as shown in Fig. 5. The isotherm of pure MC presents a typical H3 hysteresis loop (type IV) (Fig. 5A), suggesting its relatively wide mesoporous distribution, which is also confirmed by the pore size distribution (PSD) with a considerable distribution in range of 2–30 nm (Fig. 5A inset). By contrast,  $\text{CeO}_x/\text{MC-600}$  shows a type II isotherm curve with an apparently narrower PSD concentrated in range of 2–8 nm (Fig. 5B and inset). This comparison

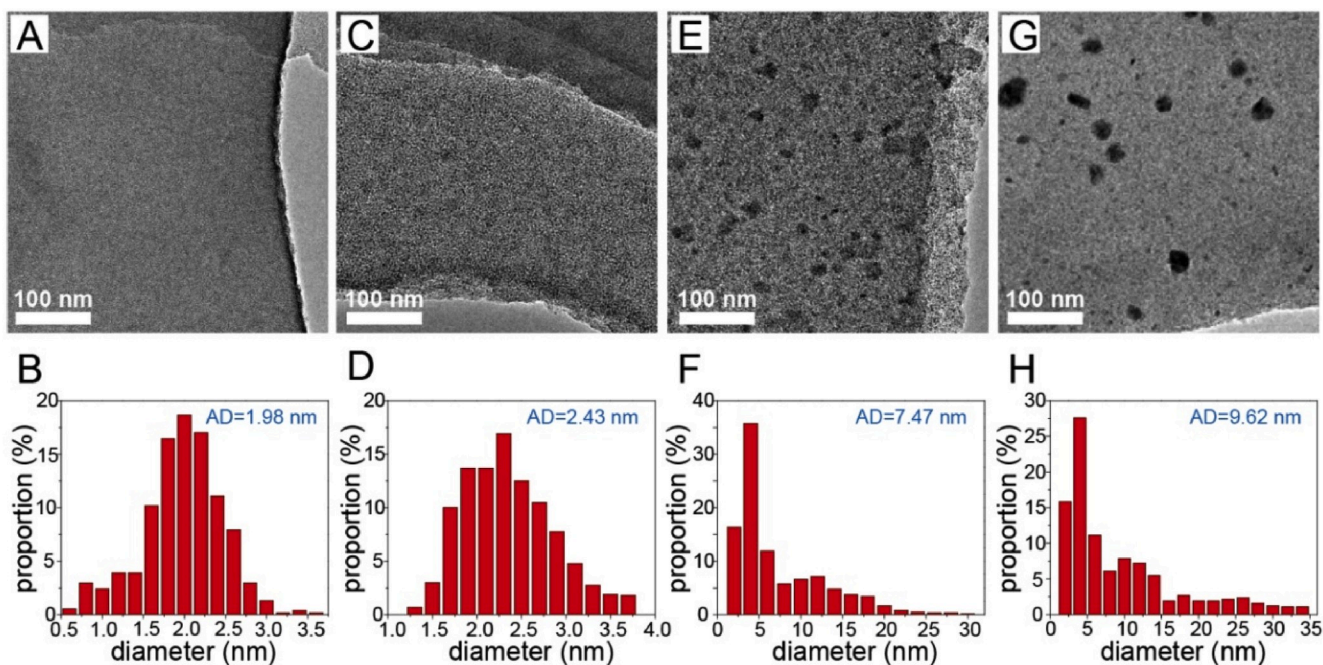


Fig. 3. TEM images and crystal size statistical analysis of  $\text{CeO}_x/\text{MC-X}$ : (A, B)  $X = 600$ , (C, D)  $X = 700$ , (E, F)  $X = 800$  and (G, H)  $X = 900$ . (AD: average diameter).

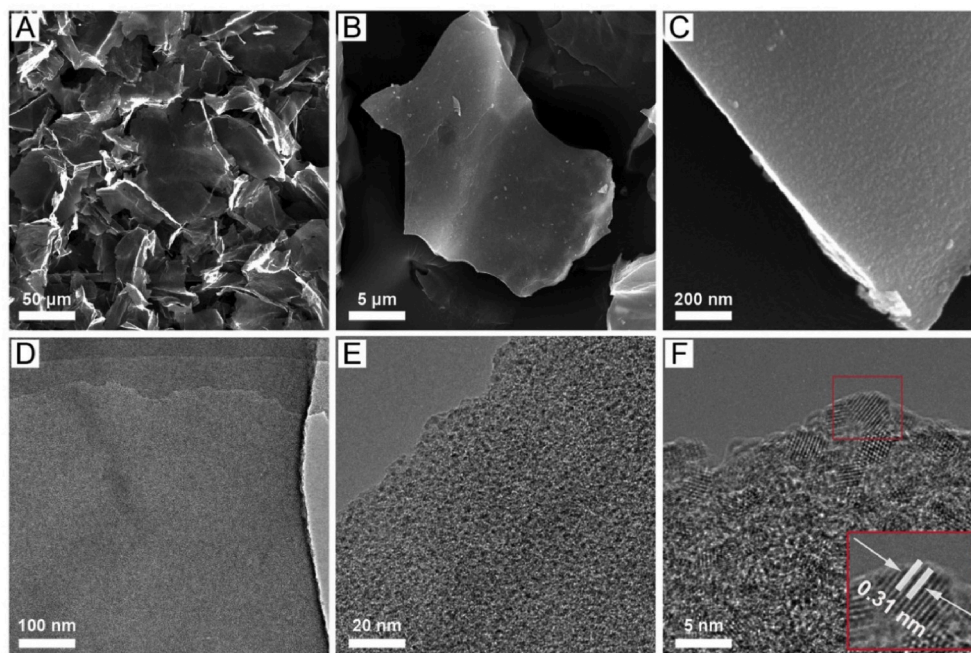


Fig. 4. (A–C) SEM and (D–F) TEM images of  $\text{CeO}_x/\text{MC-600}$  under different magnifications.

suggests that the pores of MC are considerably occupied by  $\text{CeO}_x$  nanocrystals, resulting in the specific surface areas of  $470.96$  and  $183.78 \text{ m}^2 \text{ g}^{-1}$  for pure MC and  $\text{CeO}_x/\text{MC-600}$ , respectively. In addition, the porous structures of various  $\text{CeO}_x/\text{MC-X}$  ( $X = 700, 800$  and  $900$ ) were also studied as shown in Fig. S7. The result shows that the highly porous nature can be well maintained under varied calcination temperatures, except that the serious particle agglomeration at  $900^\circ\text{C}$  causes some level of pore blockage with considerable porosity decrease.

To evaluate the catalytic performance of  $\text{CeO}_x/\text{MC-X}$  and pure MC for LOBs, two types of test modes, i.e., ultimate-capacity and limited-capacity tests, were adopted. The catalytic inactivity of the carbon

paper current collector was firstly verified to eliminate its interference on the experimental results (Fig. S8). The ORR/OER overpotentials, coulombic efficiency (CE) and capacity of the cells are greatly dependent on the intrinsic catalytic capability as well as the architectural design of the catalyst materials [47,48]. As shown in the galvanostatic ultimate-capacity test in Fig. 6A,  $\text{CeO}_x/\text{MC-600}$  exhibits an ORR overpotential of  $0.24 \text{ V}$  and an OER overpotential of  $1.41 \text{ V}$  with a resultant charge-discharge potential gap of  $1.65 \text{ V}$ . Similar overpotential can be observed for  $\text{CeO}_x/\text{MC-700}$ , while  $\text{CeO}_x/\text{MC-800}$ ,  $900$  and pure MC undergo much severer electrochemical polarizations with expanded charge-discharge potential gaps in addition to the reduced ultimate

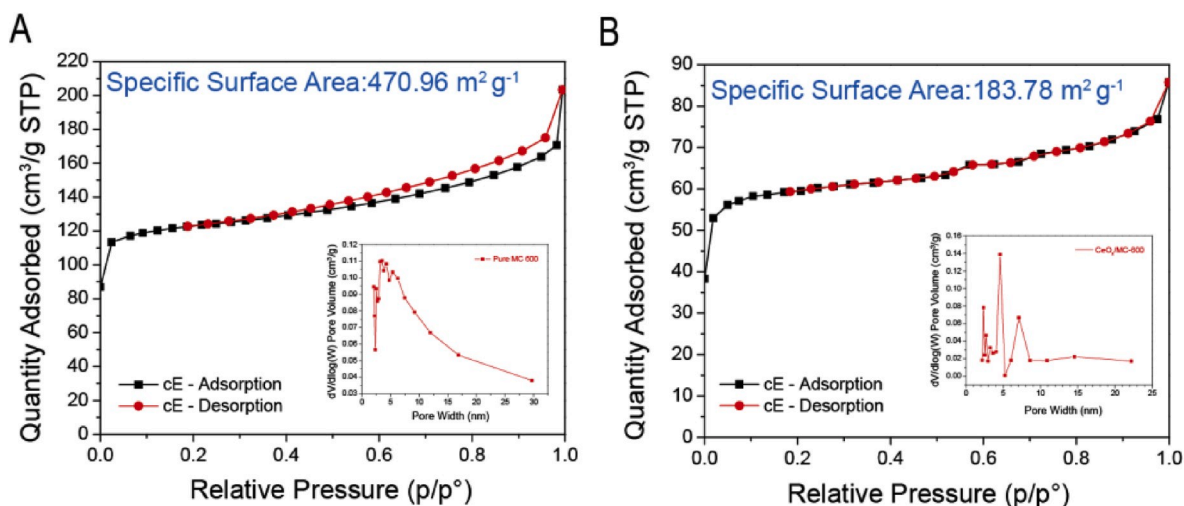


Fig. 5.  $N_2$  adsorption-desorption isotherms and pore size distribution (insets) of (A) pure MC and (B)  $CeO_x/MC-600$ .

capacities. Moreover, the CEs of  $CeO_x/MC-X$  ( $X = 600, 700, 800$  and  $900$ ) and pure MC are 92.1%, 98.8%, 70.2%, 31.5% and 71.4%, respectively, as presented in Fig. 6B. These results suggest the superior ORR/OER kinetics for  $CeO_x/MC-600$  and  $CeO_x/MC-700$  over the rest samples. The large overpotential and low CE of  $CeO_x/MC-900$ , which are even inferior to the pure MC, can be ascribed to its crystalline impurity (BCC  $CeO_{2-x}$  and  $Ce_2O_3$ ) and unfavorably large crystal size (9.6 nm in average). As a result,  $CeO_x/MC-X$  ( $X = 600, 700, 800$  and  $900$ ) and pure MC exhibit discharge capacities of 12753, 8884, 8685, 6840 and 5261  $mAh\ g^{-1}$ , respectively, manifesting the great superiority of  $CeO_x/MC-600$  as cathode catalyst for oxygen redox reactions. Additionally, the rate performance of  $CeO_x/MC-600$  was also evaluated as shown in Fig. S9. Very limited charge-discharge overpotentials and capacity loss can be observed when raising the current rate from 100 to 200 and 300  $mA\ g^{-1}$ , suggesting a good rate capability of the according LOB. This is mainly attributed to its combination of highly porous architecture that favors the fast electron/ion transfer, as well as the ultrafine distribution of  $CeO_x$  nanocrystals that enables efficient exposure of active surface, which synergistically contributes to a fast and efficient oxygen electrochemistry.

In addition, the cycling performance was evaluated under the limited-capacity mode with a controlled capacity of  $1000\ mAh\ g^{-1}$  at a current density of  $200\ mA\ g^{-1}$  (Fig. 6C–F). It can be clearly observed that  $CeO_x/MC-600$  exhibits a significantly smaller potential gap between ORR and OER curves than that for pure MC (Fig. 6D), which is consistent with the results in ultimate-capacity test. More importantly, the  $CeO_x/MC-600$  cell maintains a continuous 55 charge-discharge cycles with a constantly high CE close to unity (Fig. 6E). By contrast, pure MC fails to proceed reversible cycling over 11 cycles (Fig. 6F), since where both capacity and CE rapidly decrease ascribed to the poor oxygen redox kinetics and electrochemical reversibility. It should be noted that these performances are highly competitive among the ceria-based electrode materials in recent literature as shown in Table S3, which further manifests the structural superiorities of this design.

To illustrate the effect of  $CeO_x$  particle size on catalytic performance, cycling characterizations were also performed for various  $CeO_x/MCs$  as shown in Fig. S10. It can be perceived that the overpotential and cyclability of the cells continuously deteriorate along with the increase of particles size in  $CeO_x/MC-X$ , which is consistent with the above results. The reversible cycling can be sustained until 50, 40, and 26 cycles for  $CeO_x/MC-700, 800$  and  $900$ , respectively, confirming that smaller crystal size and more dispersive  $CeO_x$  contribute to higher LOB performance. Apart from that, the impact of oxygen-deficiency and  $CeO_x$  loading on the catalytic performance were also studied by comparing with commercial  $CeO_2$  and low-loading 1 mM- $CeO_x/MC-600$ .

Commercial  $CeO_2$  was mixed with pure MC in the same ratio with  $CeO_x/MC-600$  for the performance evaluation. As shown in Figs. S11A–C, the commercial  $CeO_2$  with less oxygen vacancies exhibits distinctly increased overpotential in both ultimate capacity and limited capacity modes as well as inferior cyclability compared with those of  $CeO_x/MC-600$ . This result strongly confirms the great effect of oxygen-deficiency in improving the reaction kinetics and redox reversibility for oxygen electrochemistry. Apart from that, the low-loading  $CeO_x/MC-600$  ( $CeO_x$  content:  $\sim 10\ wt\%$ ) prepared with a diluted cerium source was also evaluated (Figs. S11D–F), which exhibits a slightly increased redox potential gap of 1.72 V compared with that of the  $CeO_x/MC-600$  (1.65 V), but with significantly inferior electrochemical reversibility and cyclability ascribed to the lack of active sites aroused by the decrease of  $CeO_x$  content.

CV measurements were carried out for pure MC, commercial  $CeO_2$  and  $CeO_x/MC-600$  to further investigate the catalytic activity as shown in Fig. S12A. Obviously,  $CeO_x/MC-600$  exhibits considerably smaller redox peak potential gaps as well as higher current response compared with those of pure MC and commercial  $CeO_2$ , further confirming its significantly enhanced reaction kinetics due to the unique compositional and structural superiorities. Fig. S12B shows the impedance variation of the LOB cell based on  $CeO_x/MC-600$  cathode at the fresh, discharged and recharged states. It can be perceived that the discharged cell shows a significantly larger charge-transfer resistance ( $R_{ct}$ ) than that at fresh state. This likely originates from the surface passivation by the insoluble  $Li_2O_2$  products on cathode surface as verified by XRD measurement (Fig. S13), which impedes the electron/ion transfer and leads to deteriorated reaction kinetics [49,50]. The  $R_{ct}$  well recovers after recharging, confirming the good electrochemical reversibility on  $CeO_x/MC-600$  surface. For further verification, SEM observation was performed on electrode surface at different charge-discharge states as shown in Fig. 7. The results reveal that after discharging at a controlled capacity of  $1000\ mAh\ g^{-1}$ , a large amount of  $Li_2O_2$  is uniformly accumulated in forms of fine nanoparticles on the  $CeO_x/MC-600$  surface (Fig. 7 A and inset), which basically disappears after recharging (Fig. 7B). Even after 10 cycles, only a small amount of nano-precipitation can be observed as shown in Fig. 7C. Whereas on the surface of pure MC cathode, the discharge product  $Li_2O_2$  precipitates as much larger nano-islands as shown Fig. 7 D and inset, which partially remains after initial recharging and considerably accumulates after 10 cycles (Fig. 7 E and F). This comparative result strongly manifests the significantly improved oxygen reaction reversibility on the as-developed  $CeO_x/MC-600$  surface, although serious advances are still required to further improve the reaction kinetics and reversibility for high-performance LOBs. In addition, the post-cycling TEM characterization was also performed as shown in

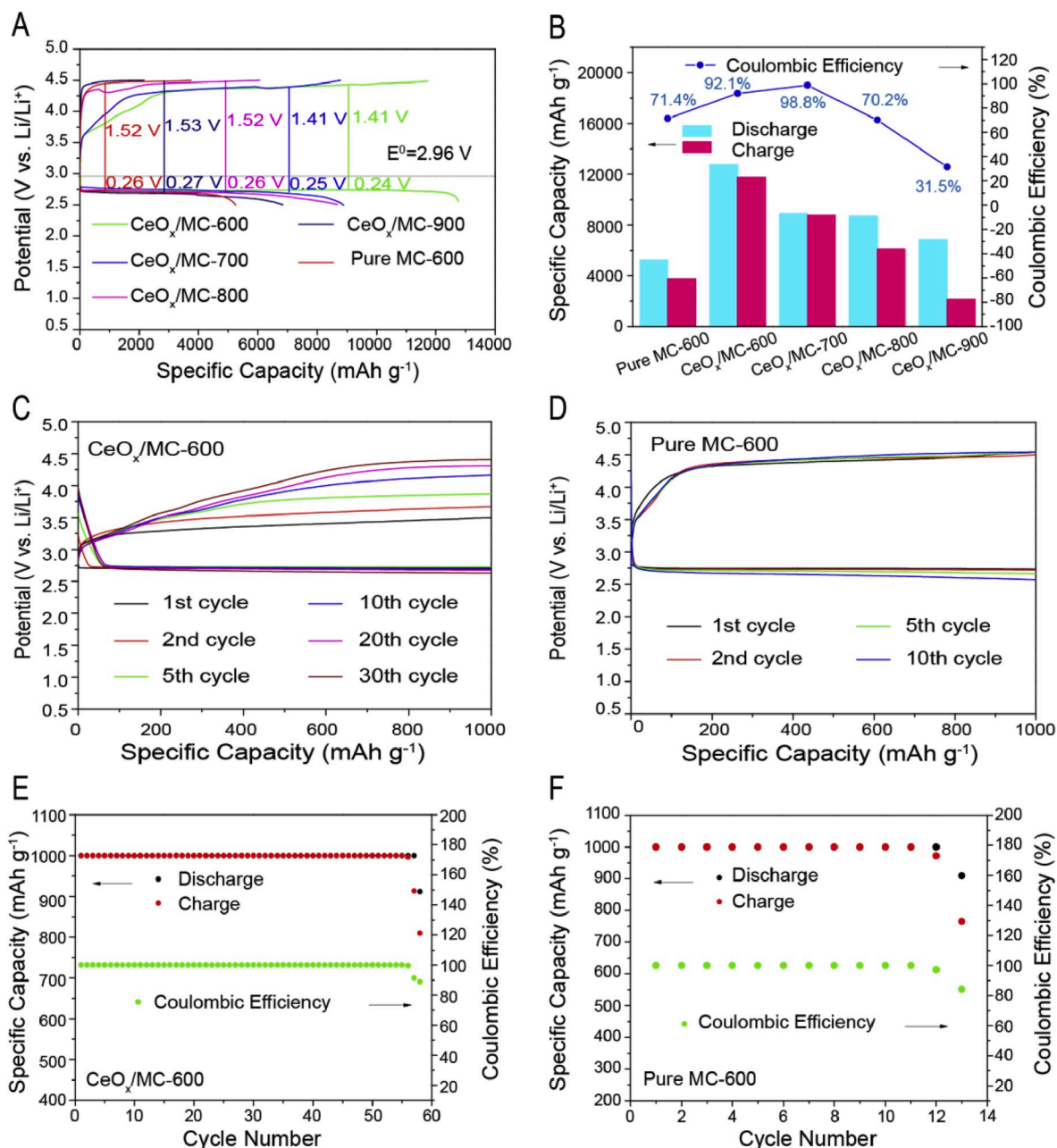


Fig. 6. Ultimate capacity tested at 100 mA g<sup>-1</sup>: (A) discharge/charge profiles and (B) capacity and Coulombic efficiency of CeO<sub>x</sub>/MC-X (X = 600, 700, 800 and 900) and pure MC. Limited capacity (1000 mAh g<sup>-1</sup>) tested at 200 mA g<sup>-1</sup>: discharge/charge profiles of (C) CeO<sub>x</sub>/MC-600 and (D) pure MC; long-term cycling performance of (E) CeO<sub>x</sub>/MC-600 and (F) pure MC.

Fig. S14, which shows well-maintained sheet-like architecture and unobservable particle agglomeration, evidentially confirming the good structural integrity of CeO<sub>x</sub>/MC-600 upon the battery cycling.

Combining the above results, we propose the improvement mechanism of the as-developed CeO<sub>x</sub>/MC for LOBs as schematically demonstrated in Fig. 8. Attributed to the ultrafine, high-loading and oxygen-deficient CeO<sub>x</sub>, the as-developed CeO<sub>x</sub>/MC-600 provides a vast amount of active sites, which facilitates the oxygen redox reactions and regulates the nucleation of the insoluble product to form uniform and fine distribution on catalyst surface. However, the lack of oxygen affinity and nucleation regulation on pure MC surface result in the messy deposition and wild growth of the insoluble products, which passivate the active surface and obstruct the electron/mass transfer pathways, thus giving rise to serious electrochemical polarization and reaction irreversibility.

#### 4. Conclusions

In summary, this work reports an ultrafine, high-loading and oxygen-deficient CeO<sub>x</sub> implanted in mesoporous carbon nanosheets for improved LOBs. The CeO<sub>x</sub>/MC was obtained via a facile impregnation and calcination method, where the x value and crystal size of CeO<sub>x</sub> linearly evolved along with the heating temperatures (600–900 °C). As a result, CeO<sub>x</sub>/MC-600 was achieved with ultrasmall crystal size of 1.98 nm in average, high CeO<sub>x</sub> loading up to 43.8 wt%, and abundant oxygen deficiency (x = 1.813), which combined efficiently-exposed active sites and massive electron/mass transfer pathways, contributing to a fast and efficient oxygen electrochemistry. LOBs based on CeO<sub>x</sub>/MC-600 delivered a high capacity of 12753 mAh g<sup>-1</sup> with coulombic efficiency of 92.1% at ultimate-capacity test, as well as a decent cyclability over 55 cycles at limited-capacity test of 1000 mAh g<sup>-1</sup>. This work shows the

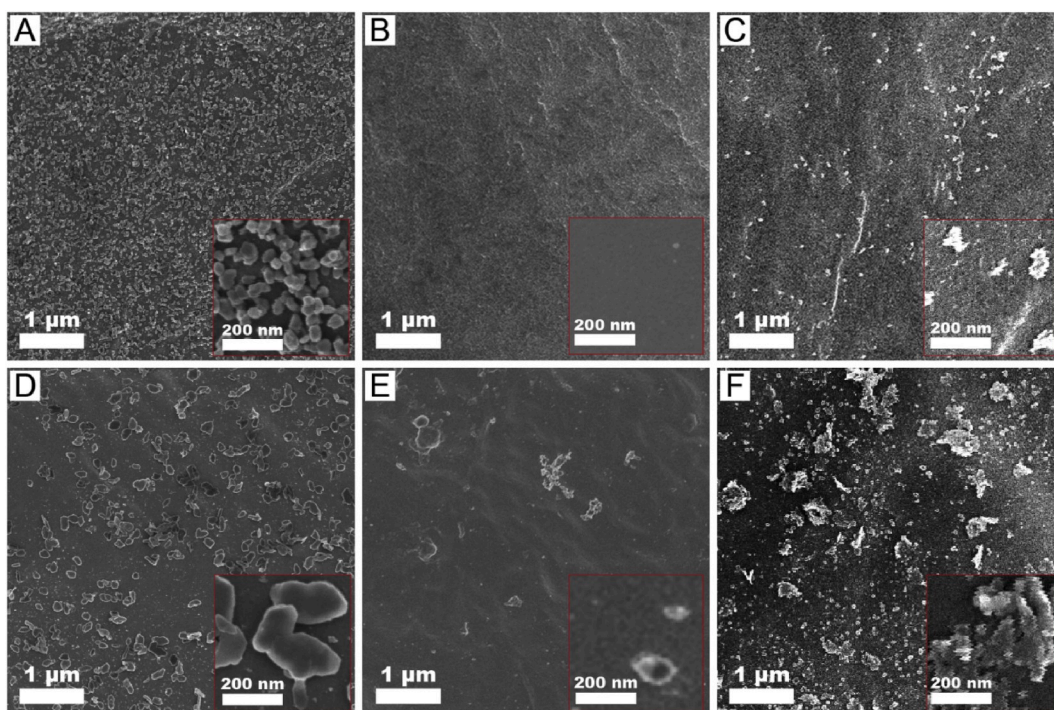


Fig. 7. SEM images of (A–C)  $\text{CeO}_x/\text{MC-600}$  and (D–F) pure MC electrodes at the end of (A, D) initial discharge, (B, E) initial charge and (C, F) 10th charge.

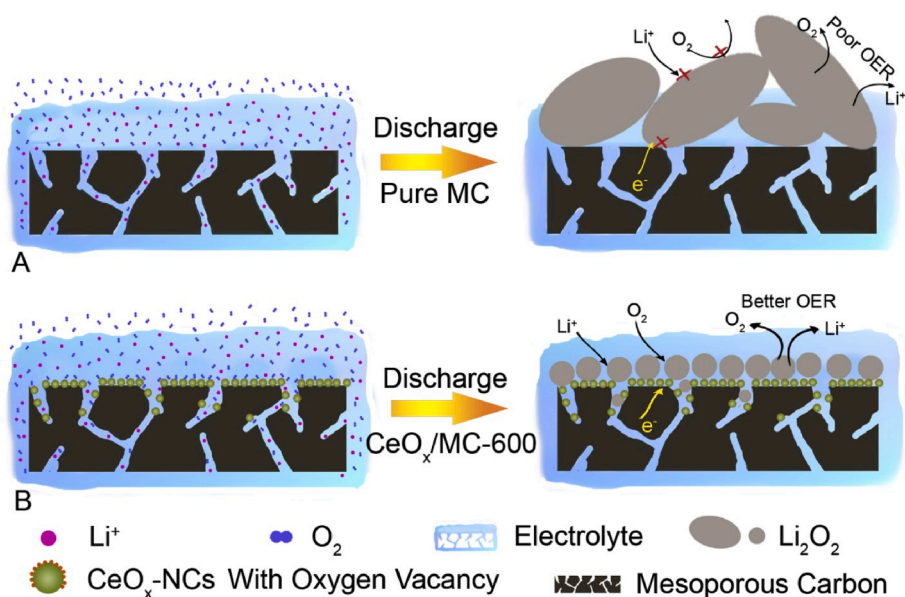


Fig. 8. Schematic diagram for the improvement mechanism of  $\text{CeO}_x/\text{MC-600}$ .

regulation and effect of oxygen vacancy, crystal size and mass loading of  $\text{CeO}_x$  on catalytic capability for LOBs, opening a new pathway to the development of advanced catalyst materials in LOBs and other related fields.

#### Declaration of competing interest

The authors declare that they have no known competing financial interests or personal relationships that could have appeared to influence the work reported in this paper.

#### Acknowledgements

This work was supported by the Natural Science Foundation of Zhejiang Province (LGG18B030001), the Key Research and Development Program of Science and Technology Department of Zhejiang Province (2017C01023). The authors also thank the supports from the Natural Sciences and Engineering Research Council of Canada (NSERC) and the University of Waterloo.

#### Appendix A. Supplementary data

Supplementary data to this article can be found online at <https://doi.org/10.1016/j.nanoen.2020.104570>.

org/10.1016/j.nanoen.2020.104570.

## References

- [1] J. Wang, Y. Li, X. Sun, *Nano Energy* 2 (2013) 443–467.
- [2] D. Aurbach, B. McCloskey, L. Nazar, P. Bruce, *Nat. Energy* 1 (2016) 16128.
- [3] A. Luntz, B. McCloskey, *Chem. Rev.* 114 (2014) 11721–11750.
- [4] T. Yu, J. Fu, R. Cai, A. Yu, Z. Chen, *IEEE Nanotechnol. Mag.* 11 (2017) 29–55.
- [5] L. Ma, T. Yu, E. Tzoganakis, K. Amine, T. Wu, Z. Chen, J. Lu, *Adv. Energy Mater.* 8 (2018) 1800348.
- [6] N. Feng, P. He, H. Zhou, *Adv. Energy Mater.* 6 (2016) 1502303.
- [7] D. Geng, N. Ding, T. Andy Hor, S. Chien, Z. Liu, D. Wu, X. Sun, Y. Zong, *Adv. Energy Mater.* 6 (2016) 1502164.
- [8] S. Zhang, D. Foster, J. Read, *J. Power Sources* 195 (2010) 1235–1240.
- [9] S. Zhang, K. Xu, J. Read, *J. Power Sources* 196 (2011) 3906–3910.
- [10] H. Woo, J. Kang, J. Kim, C. Kim, S. Nam, B. Park, *Electron. Mater. Lett.* 12 (2016) 551–567.
- [11] B. Sun, L. Guo, Y. Ju, P. Munroe, E. Wang, Z. Peng, G. Wang, *Nano Energy* 28 (2016) 486–494.
- [12] C. Shu, C. Wu, J. Long, H. Guo, S. Dou, J. Wang, *Nano Energy* 57 (2019) 166–175.
- [13] F. Gittleston, W. Ryu, M. Schwab, X. Tong, A. Taylor, *Chem. Commun.* 52 (2016) 6605–6608.
- [14] Y. Lai, W. Chen, Z. Zhang, Y. Qu, Y. Gan, J. Li, *Electrochim. Acta* 191 (2016) 733–742.
- [15] S. Sankarasubramanian, N. Singh, F. Mizuno, J. Prakash, *J. Power Sources* 319 (2016) 202–209.
- [16] J. Wu, H. Park, A. Yu, D. Higgins, Z. Chen, *J. Phys. Chem. C* 116 (2012) 9427–9432.
- [17] C. Hou, J. Han, P. Liu, C. Yang, G. Huang, T. Fujita, A. Hirata, M. Chen, *Nano Energy* 47 (2018) 427–433.
- [18] M. He, P. Zhang, S. Xu, X. Yan, *ACS Appl. Mater. Interfaces* 8 (2016) 23713–23720.
- [19] G. Zhao, R. Mo, B. Wang, L. Zhang, K. Sun, *Chem. Mater.* 26 (2014) 2551–2556.
- [20] A. Eftekhari, B. Ramanujam, *J. Mater. Chem.* 5 (2017) 7710–7731.
- [21] D. Higgins, Z. Chen, D. Lee, Z. Chen, *J. Mater. Chem.* 1 (2013) 2639.
- [22] C. Cao, J. Xie, S. Zhang, B. Pan, G. Cao, X. Zhao, *J. Mater. Chem.* 5 (2017) 6747–6755.
- [23] Y. Yang, C. Tian, L. Sun, R. Lü, W. Zhou, K. Shi, K. Kan, J. Wang, H. Fu, *J. Mater. Chem.* 1 (2013) 12742.
- [24] X. Li, Z. Li, X. Yang, L. Jia, Y. Fu, B. Chi, J. Pu, J. Li, *J. Mater. Chem.* 5 (2017) 3320–3329.
- [25] J. Liu, M. Dai, T. Wang, P. Sun, X. Liang, G. Lu, K. Shimano, N. Yamazoe, *ACS Appl. Mater. Interfaces* 8 (2016) 6669–6677.
- [26] S. Agarwal, X. Zhu, E. Hensen, B. Mojte, L. Lefferts, *J. Phys. Chem. C* 119 (2015) 12423–12433.
- [27] X. Lin, L. Zhou, T. Huang, A. Yu, *J. Mater. Chem.* 1 (2013) 1239–1245.
- [28] Z. Guo, D. Zhou, X. Dong, Z. Qiu, Y. Wang, Y. Xia, *Adv. Mater.* 25 (2013) 5668–5672.
- [29] Z. Wang, D. Xu, J. Xu, L. Zhang, X. Zhang, *Adv. Funct. Mater.* 22 (2012) 3699–3705.
- [30] H. Gong, H. Xue, T. Wang, H. Guo, X. Fan, L. Song, W. Xia, J. He, *ACS Appl. Mater. Interfaces* 8 (2016) 18060–18068.
- [31] Y. Zhang, X. Wang, J. Yin, Y. Wang, C. Li, D. Xia, *Chemistryselect* 4 (2019) 4593–4597.
- [32] Y. Hou, J. Wang, J. Liu, C. Hou, Z. Xiu, Y. Fan, L. Zhao, Y. Zhai, H. Li, J. Zeng, X. Gao, S. Zhou, D. Li, Y. Li, F. Dang, K. Liang, P. Chen, C. Li, D. Zhao, B. Kong, *Adv. Energy Mater.* (2019) 1901751.
- [33] F. Vasiliu, V. Parvulescu, C. Sarbu, *J. Mater. Sci.* 29 (1994) 2095–2101.
- [34] A. Tok, F. Boey, Z. Dong, X. Sun, *J. Mater. Process. Technol.* 190 (2007) 217–222.
- [35] Y. Yu, X. Wang, W. Gao, P. Li, W. Yan, S. Wu, Q. Cui, W. Song, K. Ding, *J. Mater. Chem.* 5 (2017) 6656–6663.
- [36] X. Li, Z. Liu, L. Song, D. Wang, Z. Zhang, *Electrochim. Acta* 263 (2018) 561–569.
- [37] Y. Jiang, L. Zou, J. Cheng, Y. Huang, Z. Wang, B. Chi, J. Pu, J. Li, *J. Power Sources* 400 (2018) 1–8.
- [38] Y. Jiang, J. Cheng, L. Zou, X. Li, Y. Huang, L. Jia, B. Chi, J. Pu, J. Li, *ChemCatChem* 9 (2017) 4231–4237.
- [39] C. Yang, R. Wong, M. Hong, K. Yamanaka, T. Ohta, H. Byon, *Nano Lett.* 16 (2016) 2969–2974.
- [40] Y. Zhao, L. Zheng, H. Wu, H. Chen, L. Su, L. Wang, Y. Wang, M. Ren, *Electrochim. Acta* 282 (2018) 609–617.
- [41] L. Wang, F. Yin, C. Yao, *Int. J. Hydrogen Energy* 39 (2014) 15913–15919.
- [42] J. Han, J. Meeprasert, P. Maitarad, S. Nammuangruk, L. Shi, D. Zhang, *J. Phys. Chem. C* 120 (2016) 1523–1533.
- [43] H. Byon, B. Gallant, S. Lee, Y. Shao-Horn, *Adv. Funct. Mater.* 23 (2013) 1037–1045.
- [44] H. Zhao, Y. Dong, P. Jiang, G. Wang, J. Zhang, *ACS Appl. Mater. Interfaces* 7 (2015) 6451–6461.
- [45] S. Phokha, S. Hunpratub, B. Usher, A. Pimsawat, N. Chanlek, S. Maensiri, *Appl. Surf. Sci.* 446 (2018) 36–46.
- [46] Y. Zeng, X. Xiong, D. Wang, L. Wu, *J. Mater. Process. Technol.* 214 (2014) 3150–3157.
- [47] Z. Wen, C. Shen, Y. Lu, *Chempluschem* 80 (2015) 270–287.
- [48] Z. Ma, X. Yuan, L. Li, Z. Ma, D. Wilkinson, L. Zhang, J. Zhang, *Energy Environ. Sci.* 8 (2015) 2144–2198.
- [49] M. Hong, H. Choi, H. Byon, *Chem. Mater.* 27 (2015) 2234–2241.
- [50] C. Shu, J. Wang, J. Long, H. Liu, S. Dou, *Adv. Mater.* (2019) 1804587.